Geophys. J. Int. (1996) **127**, 719–727

Free-surface formulation of mantle convection—II. Implication for subduction-zone observables

Michael Gurnis, Christophe Eloy* and Shijie Zhong
Seismological Laboratory, California Institute of Technology, Pasadena, CA 91125, USA

Accepted 1996 August 9. Received 1996 August 5; in original form 1995 November 22

SUMMARY

Viscous and viscoelastic models for a subduction zone with a faulted lithosphere and internal buoyancy can self-consistently and simultaneously predict long-wavelength geoid highs over slabs, short-wavelength gravity lows over trenches, trench–forebulge morphology, and explain the high apparent strength of oceanic lithosphere in trench environments. The models use two different free-surface formulations of buoyancy-driven flows (see, for example, Part I): Lagrangian viscoelastic and pseudo-free-surface viscous formulations. The lower mantle must be stronger than the upper in order to obtain geoid highs at long wavelengths. Trenches are a simple consequence of the negative buoyancy of slabs and a large thrust fault, decoupling the overriding from underthrusting plates. The lower oceanic lithosphere must have a viscosity of less than 10^{24} Pa s in order to be consistent with the flexural wavelength of forebulges. Forebulges are dynamically maintained by viscous flow in the lower lithosphere and mantle, and give rise to apparently stiffer oceanic lithosphere at trenches. With purely viscous models using a pseudo-free-surface formulation, we find that viscous relaxation of oceanic lithosphere, in the presence of rapid trench rollback, leads to wider and shallower back-arc basins when compared to cases without viscous relaxation. Moreover, in agreement with earlier studies, the stresses necessary to generate forebulges are small (~ 100 bars) compared to the unrealistically high stresses needed in classic thin elastic plate models.

Key words: fault models, geoid, mantle convection, rheology, subduction, topography.

1 INTRODUCTION

Subducting lithosphere at converging plate margins is associated with long-wavelength geoid and free-air gravity highs on wavelengths of 10^3 to 10^4 km (Kaula 1972), while on wavelengths of about 200 km and smaller there are geoid and free-air gravity lows directly correlated with deep and narrow oceanic trenches (Heiskanen & Vening Meinesz 1958). Oceanic trenches are about 100 km wide, 2 to 4 km deep, and often associated with forebulges (topographic highs 100–200 km oceanwards of the trenches) (Watts & Talwani 1974). The depths of oceanic trenches increase with age of the lithosphere just prior to subduction (Hilde & Uyeda 1983), plate convergence rate (Grellet & Dubois 1982), and intermediate-depth (e.g. depths less than 100 km) Benioff-zone dip (Jarrad 1986). The distance from the maximum trench depth to forebulge high, a measure proportional to the flexural parameter, increases with lithospheric age (Watts, Bodine & Ribe 1980; McAdoo, Martin & Poulouse 1985). These observations together point to complex, wavelength-dependent compensation with forces and strength increasing with plate age. Working out the coupling between long and short wavelengths in a converging margin is a fundamental goal of geophysics.

Although, in the early days, Griggs (1972) tried to integrate the long- and short-wavelength gravitational field over subduction zones, in the decades following the recognition that oceanic trenches were the site of plate consumption, two independent lines of research developed: one which we call flexural studies, the other geodynamic studies. The flexural studies deal with the shorter-wavelength characteristics of the oceanic lithosphere and forebulges. Geodynamic studies deal with the long-wavelength geoid in terms of viscous flow in the mantle. We believe that these two approaches can ultimately be merged with more realistic formulations; the present work builds upon that of Zhong, Gurnis & Moresi (this issue; hereafter referred to as Part I).

Flexural studies deal with the rheological characteristics of the lithosphere and the forces acting at plate margins by fitting observed trench–forebulge bathymetry, gravity, and geoid

* Now at: Ecole Normale Superieure, 45. rue d'Ulm, 75005 Paris, France.

profiles with thin-plate models incorporating a few (usually one) lithospheric strength parameters (for example Watts & Talwani 1974; Caldwell *et al.* 1976; Parsons & Molnar 1976; McAdoo, Caldwell & Turcotte 1978). These formulations usually assume that the oceanic lithosphere is elastic or elasto-plastic and that the sublithosphere is inviscid. In a provocative paper, De Bremaecker (1977) showed that the classical trench–forebulge topography could be generated by a thin viscous plate overlying an inviscid mantle. He argued that the best fit to the bathymetry was found for a 120 km thick lithosphere with a viscosity of 10^{23} Pa s (at the Mariana trench). Besides the rheology, De Bremaecker's formulation differed fundamentally from elastic ones in that lithosphere explicity moves towards the trench at a fixed velocity. An implication is that forebulges are transient features.

With an extensive compilation of elastic and mechanical thicknesses inferred for the oceanic lithosphere, Wessel (1992) argued that the effective mechanical thickness of the lithosphere is dependent on how the lithosphere is deformed. He argued that the plate is approximately twice as thick when responding to trench-induced flexure compared to the response of seamount loading. Earlier, McAdoo *et al.* (1985) had shown that old oceanic lithosphere at trenches was strong; indeed, McAdoo's geoid-inferred elastic lithosphere thicknesses tend to be twice that presented in a compilation by Watts *et al.* (1980).

Returning to the larger-scale structure, Griggs (1972) showed that long-wavelenth geoid highs over subduction zones may be caused by the gravitational pull of the cold and heavy slab, but that there must be regional compensation due to viscous flow; he approximated the regional compensation by a simple cosine curve which he adjusted to obtain the observed geoid. He assumed that the gravity of trenches was caused by trench topography. By summing the two components, he could obtain observed gravity profiles. The Griggs model was entirely heuristic in that it lacked the physics which connected the ultimate driving force, the negative buoyancy of slabs, to the final topographic and gravitational structure.

Hager (1984) resolved the long-wavelength compensation problem posed earlier. He showed that viscous flow in the mantle associated with cold and heavy slabs would deform the Earth's surface (dynamic topography) downwards by ~ 1 km over a ~ 4000 km scale. Futhermore, a constant-viscosity mantle (constant from upper to lower mantle) would generate so much dynamic topography that the positive geoid of the dense slab would be overwhelmed, resulting in a geoid low. Hager (1984) determined that an increase in viscosity from the upper to lower mantle ($30\times$ to $300\times$) would lead to less dynamic topography and only partial compensation of the geoid, leading to the requisite geoid highs.

Dynamic viscous models of the slab geoid are fundamentally deficient because superimposed on the predicted long-wavelength geoid highs are geoid lows ~ -20 m and 500 km in width directly above slabs (Zhong & Gurnis 1992; Moresi & Gurnis 1996). These geoid and topographic lows are quite unlike observed trenches (100 km across, ~ 4 km deep and with -10 m geoids). Such dynamic, viscous-flow models are incapable of reproducing any of the features associated with trench–forebulge structure.

Implicit in the original work of Griggs (1972) is that the processes associated with deep trenches and the long-wavelength gravitational field are intimately coupled. The present study attempts to synthesize flexural and geodynamic approaches with a self-consistent formulation. This work follows on from that of Zhong & Gurnis (1992, 1994) with the following improvements: relaxation of surface topography is explicitly accounted for using the free-surface formulations introduced in Part I. Here we use a viscoelastic formulation since past studies suggest that both lithospheric viscosity and elastic strength will probably influence trench–forebulge structure. We will explicitly explore forebulge structure and its time dependence while simultaneously predicting the geoid at short and long wavelengths.

2 MODEL SET-UP

Two methodologies are used to track the growth and decay of surface topography in buoyancy-driven flows, as discussed in Part I. The first set of models uses a Lagrangian formulation [e.g. TECTON, a finite-element code (Melosh & Raefsky 1980)]. The models are realistic in terms of layered material properties of the lithosphere, but are only integrated for a few million years in order to avoid highly deformed finite-element meshes. The second set of models attempts to rectify this deficiency of short integration times with a Eulerian pseudo-free-surface method (see Part I), which uses a viscous constitutive relation. With the latter method we can study continuous subduction and trench rollback self-consistently.

In linear viscoelastic problems, where the material is subject to an initial stress or displacement, the stresses decay with a time constant $\tau_M = \mu/G$, which is often called the Maxwell time, where G is the shear modulus and μ is the dynamic viscosity. The Maxwell time is not the only characteristic timescale of this system. The Lagrangian finite-element solution, with an explicit time solver (Melosh & Raefsky 1980) allows for boundaries to deform. As described in Part I, this relaxation time is analogous to that in postglacial rebound, except that now we have a coupled internal–surface loading problem, whereas postglacial rebound is strictly a surface loading problem (e.g. Cathles 1975). This highlights the second major difference from our earlier work on subduction zones (Zhong & Gurnis 1992, 1994) besides the incorporation of elasticity: the relaxation of free surfaces. The earlier work assumed that surface topography was always in equilibrium with stresses generated by Stokes flow. This assumption of equilibrium may not be valid for $\sim 10^2$ km length scales (e.g. Part I) typified by trench and back-arc topography.

An essential attribute of subduction-zone dynamics is the fault which cuts or decouples subducting from overriding plates. Ultimately, it is this feature, together with the rheology, which causes the subduction to have two fundamentally different length scales, as discussed above. In the current formulation, we have used the 'slippery-node' fault algorithm incorporated into the TECTON software (Melosh & Williams 1989). This slippery-node method is analogous to a dipping, free-slip internal interface and is comparable to purely viscous results (Zhong & Gurnis 1994). The free-slip internal interface is incorporated into our second set of models.

A limitation of the Lagrangian TECTON formulation of this problem is that we must restrict integration times to less than about five million years. For much longer integration times, with a purely viscous formulation, Zhong & Gurnis (1995a) showed that, when the fault is allowed to interact dynamically with the flow, rapid trench rollback is a dominant

attribute of converging margin dynamics. This is consistent with plate-tectonic reconstructions. Consequently we will use the pseudo-free-surface method introduced in Part I together with Cartesian versions of the Zhong & Gurnis (1995a) type to explore long-timescale phenomena unobtainable with TECTON. These models use much simpler representations of the lithosphere than do TECTON models. Essentially, we will explore the role of topographic relaxation in the presence of continuous subduction and self-consistent trench rollback.

2.1 Viscoelastic model set-up

In the viscoelastic models, the total area is divided into domains (Fig. 1) which are all viscoelastic. The subduction zone is modelled by a dense slab and a faulted lithosphere. The model parameters are the elastic and viscous properties of the materials and the geometry of the slab, the fault, and the different layers.

The presence of a fault with internal buoyancy poses some problems for the viscoelastic formulation. The initial response of an internally loaded, compressible viscoelastic material, as usually formulated, is self-compression. Self-compression of a domain with a faulted top surface will lead to localized deformation near the fault. We have reduced the magnitude of this problem by setting element densities, except those associated with the slab, to zero. This eliminates nearly all the self-compression. However, with zero density, there is no isostatic restoring force associated with the displacement of the top surface. A vertical surface force associated with the topography was added to each node of the surface, the force being proportional to $\Delta\rho_s g w(x)$, where $\Delta\rho_s$ is the density difference across the top surface, g is the acceleration due to gravity, and $w(x)$ is the local topography.

We formulated a reference model with five layers (Fig. 1): the upper lithosphere, the lower lithosphere, the upper mantle, the transition zone, and the lower mantle (Table 1). The upper lithosphere is essentially elastic on the timescales considered. The depth of 100 km corresponds to the thermal thickness of the lithosphere and will be varied in subsequent cases. To this layered model is added a slab with a higher density (as it is colder) and with a viscosity equal to the surrounding material [e.g. a weak slab (Moresi & Gurnis 1996)]. The slab is separated into two parts: the upper slab and the lower slab. The lower slab extends 100 km deeper than the viscosity boundary at 670 km. The slab thickness is the same as the

Table 1. Parameters of viscoelastic reference and viscous pseudo-free-surface models.

		Viscoelastic Reference Model			Pseudo Free Surface
Layer	Depth (km)	Viscosity (Pa s)	Maxwell time	Density (kg m^{-3})	Viscosity (Pa s)
Upper Lithosphere (UL)	0-30	10^{26}	38My	0	2×10^{23}
Lower Lithosphere (LL)	30-100	10^{23}	38ky	0	2×10^{23}
Upper Mantle (UM)	100-410	10^{21}	380yr	0	4×10^{20}
Transition Zone (TZ)	410-670	10^{22}	3.8ky	0	4×10^{21}
Lower Mantle (LM)	670-1500	3×10^{22}	11.4ky	0	2×10^{22}
Upper Slab (US)	100-300	10^{21}	380ky	40	--
Lower Slab (LS)	300-770	10^{22}	38ky	40	--

lithospheric thickness, and the slab dip angle, θ_S, is 60°. The weak zone, introduced at the right side, decouples the plate from the fixed boundary and allows free movement of the subducting plate. A 'slippery-node' fault is introduced through the lithosphere with a dip angle, θ_F, of 30°.

Within the lithosphere, there are two viscosity boundaries implicitly associated with conductive cooling. For the lithosphere, we assume a cooling, semi-infinite half-space. For a 150 Myr old lithosphere (assuming a thermal diffusivity of 10^{-6} m^2 s^{-1}), the depths of the 400 °C and 1000 °C isotherms are 30 km and 100 km, respectively. In the reference model, the upper lithosphere (0–400 °C) has a viscosity of 10^{26} Pa s with a 38 Myr Maxwell time that is much longer than the total integration time (5 Myr). The viscosity of the lower lithosphere (400–1000 °C) within the reference model is 10^{23} Pa s, a value suggested by Walcott (1970). The viscosity of the upper mantle is 10^{21} Pa s while the viscosity of the lower mantle is 30 times larger than the upper mantle, as suggested from studies of the geoid (Hager 1984). For all domains, a linear Newtonian viscosity was used.

A 7700-element mesh was used and the size of each element was about 30 × 30 km, with higher resolution within the slab and lithosphere (Fig. 2). The reference model was integrated for 5 Myr with a time step of 50 kyr. Resolution tests were carried out to ensure convergence. The background density was set to zero and the density of the slab was 40 kg m^{-3}. The upper lithosphere is assumed to be covered by water, so that the total force, f_b, applied on each node along the top surface is $f_b = g(\rho_m - \rho_w)w(x)\Delta x$, where g, ρ_m and ρ_w are defined in Table 2, $w(x)$ is the elevation of the node, and Δx is the

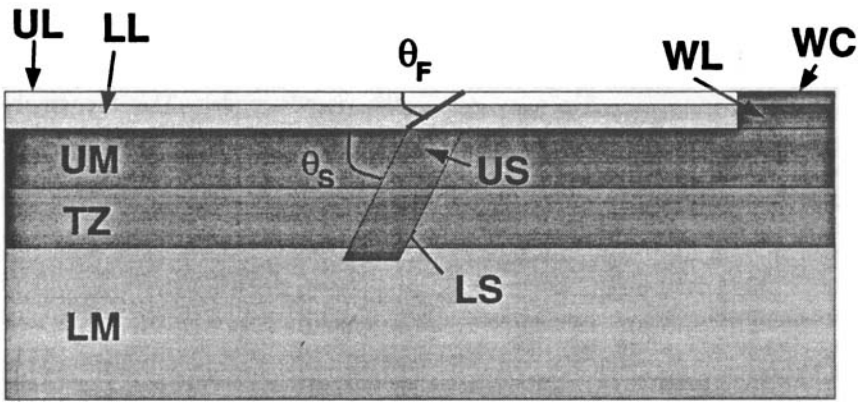

Figure 1. Geometry of the viscoelastic models showing the location of the fault and the nine domains defined in Table 1.

Table 2. Parameters held constant for viscoelastic models.

Name	Symbol	Value
Young's modulus	E	1.75×10^{11} Pa
Poisson's ratio	ν	0.3
Mantle density	ρ_m	3300 kg m^{-3}
Water density	ρ_w	1000 kg m^{-3}
Gravity acceleration	g	10 m s^{-2}
Dynamic viscosity	μ	10^{21}-10^{26} Pa s
Slab dip angle	θ_S	60 °
Fault dip angle	θ_F	30 °

horizontal distance between nodes. Except for the free surface, the boundary conditions are free-slip with the normal displacement set to zero.

2.2 Pseudo-free-surface method

We set up additional models using the pseudo-free-surface method developed in Part I. This method allows us to consider the influence of trench rollback and continuous subduction. These viscous models include a dynamically migrating faulted plate margin and a subducting slab that moves both horizontally and vertically (Zhong & Gurnis 1995a,b). Compared to the Lagrangian viscoelastic models, these models couple the solution of the momentum equation with an energy equation (see Part I for details). The energy equation allows continuous subduction to develop, i.e. cold lithosphere continuously fluxes towards the fault.

A 9000 km by 3000 km Cartesian domain with 200×80 bi-linear elements is used, with element refinement near plate margins and lithosphere. A fault extending down to the bottom of a plate (100 km) with an initial dip angle of 30° is used to represent a converging plate margin and is initially located at 5700 km from the left sidewall. Overriding the fault is a continent with a constant length of 3150 km, while the remaining surface is cooling oceanic lithosphere. Initially, the interior is isothermal (1600 °C) and an initial oceanic plate (i.e. a thermal boundary layer with an implicit plate speed of 6 cm yr^{-1}) is included. Within the continent there is no horizontal gradient in temperature. At the diverging margin of the overriding plate (from $x = 8850$ km to 9000 km), a high temperature is set initially to mimic continental rifting. In order to have a plate velocity of about 5 cm yr^{-1}, additional buoyancy with a maximum temperature anomaly of 40 K is included in the lower mantle beneath the continent and in the upper mantle beneath the oceanic plate (Zhong & Gurnis 1995a). The continent, oceanic plates, and mantle have different rheologies. For regions below 410 km depth, we use a Newtonian rheology, whereas for shallower regions excluding the continent, we adopt a power-law rheology with $n = 3$. The lithosphere, upper mantle, and lower mantle all have temperature-dependent viscosities. The rheological parameters are set to those in Table 1 of Zhong & Gurnis (1995a), and are slightly different from those used above (Table 1). The non-subducting continents are simulated with a constant 10^{25} Pa s viscosity. We use isothermal boundary conditions on both the top and bottom boundaries and free-slip on the bottom boundary; the top boundary has either a free-slip of a free-surface boundary condition. Reflecting boundary conditions are used on the sidewalls.

3 RESULTS

3.1 Viscoelastic reference model

The viscoelastic results are consistent with earlier viscous models assuming equilibrium dynamic topography (Zhong & Gurnis 1994). The introduction of a weak zone at the right boundary decouples the subducting plate from the side boundary, giving a constant velocity of about 3 mm yr^{-1}. The oceanic plate moves quite slowly for a 150 Myr slab because the oceanic lithosphere is strong and cannot efficiently turn the corner, even with a weak fault, consistent with the Newtonian viscous models (Zhong & Gurnis 1994). For times greater than ~2 Myr, the topography is qualitatively the same as deduced in purely viscous models with an analogous free-slip fault and free-slip top boundary (Zhong & Gurnis 1994): a deep and narrow trench on the subducting plate and a less deep, but wider, back-arc basin (Fig. 3a). The viscoelastic model has a wider and deeper trench and a better-developed forebulge compared to the viscous formulation (Fig. 4), assuming equilibrium dynamic topography (e.g. Part I). Both back-arc basin and trench depths increase with time. Moreover, there is a prominent forebulge on the oceanic plate which migrates towards the trench with time. After 5 Myr, the horizontal velocity of the overriding plate slows to zero, and the topography of the back-arc basin becomes stable at a depth of 1.5 km (Fig. 3a). Trench depth and fault displacement increase linearly with time. The average topography across the entire box increases linearly with time from −30 m (for the elastic response) to −60 m (after 5 Myr).

After a few million years, the total geoid looks realistic: there is a long-wavelength geoid high of about 20 m and a narrow, 200 km wide, −10 m geoid low centred directly over the trench (Fig. 3b). The geoids of Zhong & Gurnis (1992) come quite close to the results presented in Fig. 3(b), except for a ~200 km wide, −8 m geoid low present over the back-arc basin. In the present viscoelastic case, the geoid low in the back-arc basin (which is not observed in satellite altimeter profiles over any converging margin), has disappeared. There are two reasons why this back-arc basin topography low has disappeared. First, it takes time for the narrow basin to develop in the back-arc (Fig. 3a). Second, the topographic high above the fault is larger in the present viscoelastic models than in the viscous models. This topographic high above the fault overwhelms the signal of the topographic low in the geoid. The geoid acts as a low-pass filter over the topography.

Qualitatively, the morphology of trench–forebulge topography appears to be similar to the expected flexure of a thin elastic plate subject to an end load. Consequently, we can deduce an 'apparent' elastic thickness, T_e, of the lithosphere by fitting the topography with a simple model of plate bending (e.g. Walcott 1970). We computed a least-squares fit of the subducting-plate-model topography with the topography of a line-load model of plate bending. The thin elastic plate is bent by a line load, V_0, at $x = 0$ (no torque at the end). The bathymetric

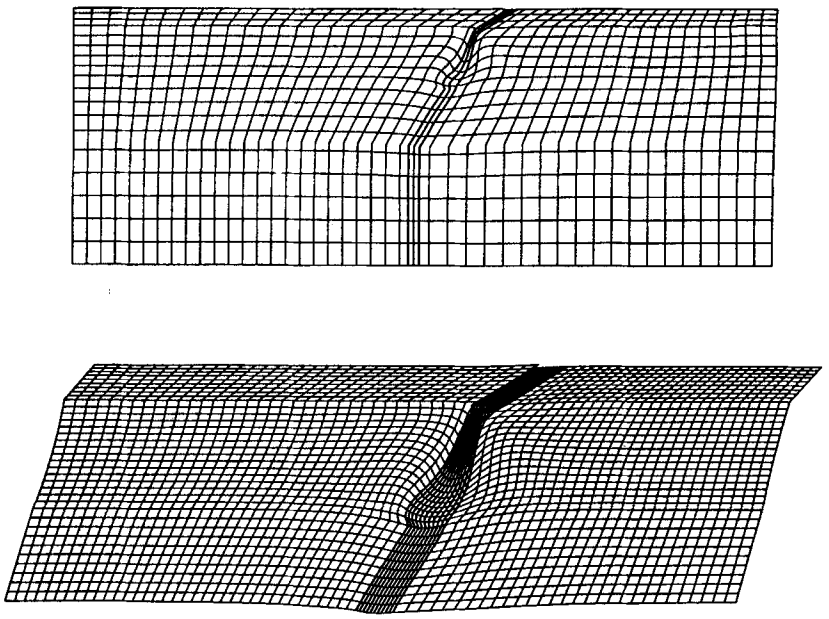

Figure 2. Location of the elements in the reference model after 5 Myr of integration. Every third element boundary is shown in the top frame, while every element is shown in the vicinity of the fault and slab, below. In the bottom figure, topographic expression is shown without vertical exaggeration.

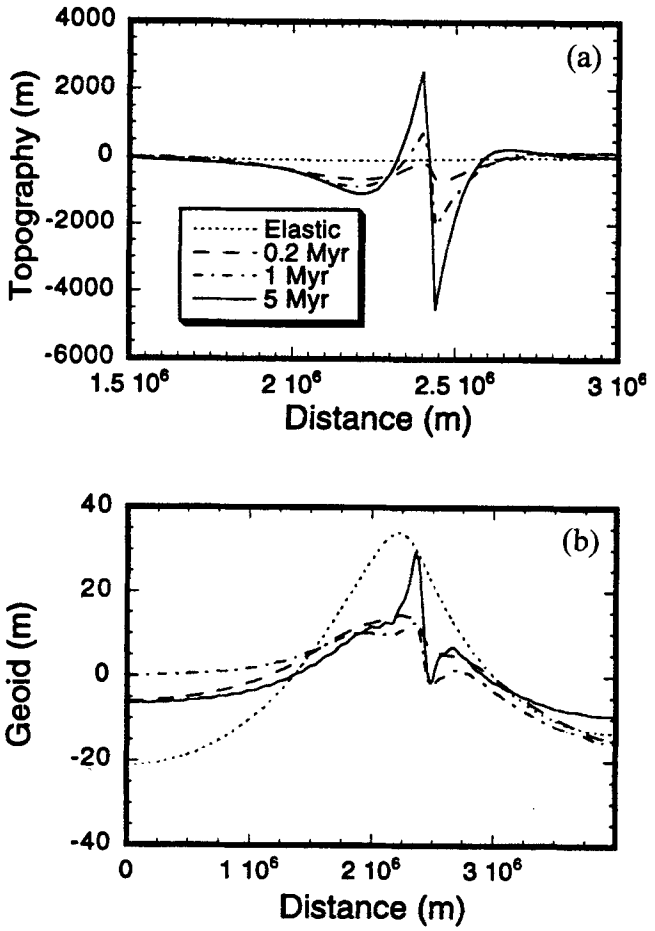

Figure 3. Topographic (a) and geoid (b) results for the reference viscoelastic model as a function of time. Note that the geoid is displayed over the whole domain while the topography is shown only in the vicinity of the fault.

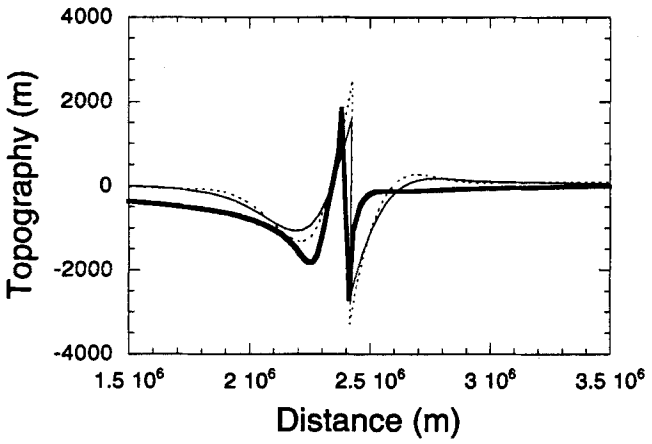

Figure 4. Comparison between a viscous solution and the corresponding viscoelastic reference model in Fig. 1 (with a single lithosphere viscosity of 10^{25} Pa s, heavy solid line) and two viscoelastic solutions after an integration time of 1 Myr (the thin solid line is the reference model, and the dotted line is identical except that the lithosphere is entirely 10^{23} Pa s).

profile of the trench is (Turcotte & Schubert 1982)

$$w(x) = \frac{\alpha^3 V_0}{2D} \exp(-x/\alpha) \cos(x/\alpha),$$

where α is the flexural parameter, $\alpha = [4D/(\rho_m - \rho_w)g]^{1/4}$, and D the flexural rigidity, $D = ET_e^3/12(1-\nu^2)$, where E is Young's modulus and ν is Poisson's ratio. Most significantly, the apparent elastic thickness of the lithosphere decreases from 85 km at 200 kyr to 35 km at 5 Myr (Fig. 5, open circles). The only layer that has a Maxwell time longer than 5 Myr is the upper lithosphere. This upper layer has an expected elastic thickness of 30 km. The viscous stresses have an important role in supporting the forebulge and make the lithosphere appear thicker.

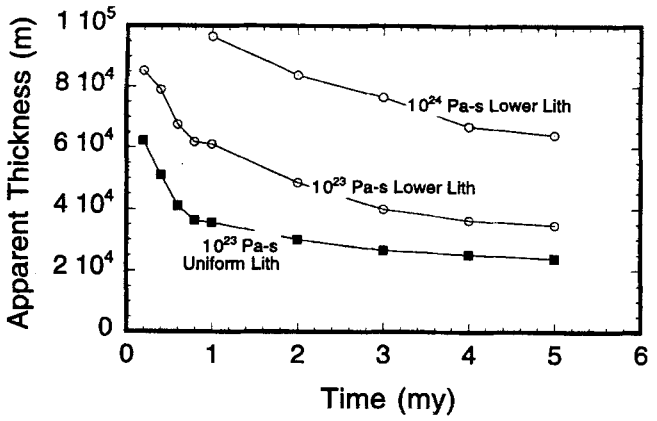

Figure 5. The change in the apparent elastic thickness of the oeanic lithosphere with viscoelastic rheologies. Open circles are for the reference model, with other cases shown for comparison.

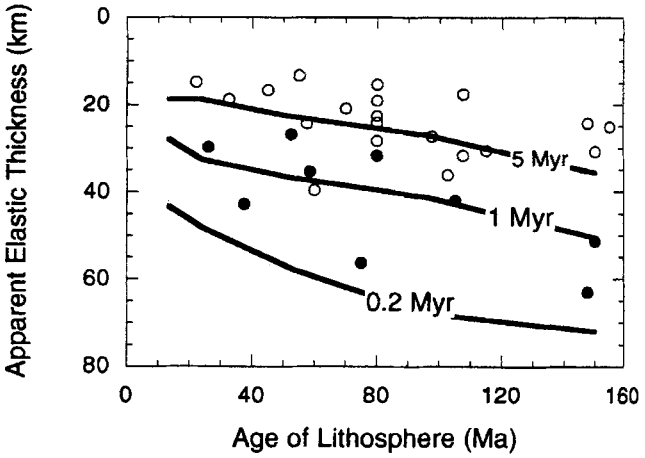

Figure 6. Age of oceanic lithosphere versus its apparent mechanical thickness at three integation times. Solid circles are for trenches (McAdoo *et al.* 1985) and open circles are mostly for seamounts (Watts *et al.* 1980).

3.2 Influence of viscoelastic parameters

Some of the features described above are dependent on lithospheric viscosity, lithospheric thickness, and fault dip. We tried to isolate the role of the viscosity of the upper lithosphere by making a model with a uniform 10^{23} Pa s lithosphere. In this case, the Maxwell times of the different materials are all less than 38 kyr, significantly less than the total integration time. The velocity field is nearly the same as the reference model, but the topography is substantially different. The back-arc basin is deeper and shows a bulge (Fig. 4, thin dotted line). The time required for the back-arc basin depth to stabilize is the same in this model as it is in the reference model. Apparently, this timescale depends on the viscosity of the lower lithosphere, which is the same in both cases. The trench depth and its time dependence in the weak-lithosphere model are nearly identical to those quantities in the reference model. The apparent elastic thickness of the lithosphere depends on the viscosity of the upper lithosphere (Fig. 5). The apparent elastic thickness comes to an equilibrium value of 25 km (10 km thinner than the reference model), but at a rate not significantly different from that in the reference model (Fig. 5, solid squares). Apparently, forebulge relaxation is being controlled more by lower-lithosphere viscosity than upper; however, the upper-lithosphere viscosity does influence the final equilibrium bulge configuration. It is quite clear that an oceanic lithosphere that has a high-viscosity lower component will lead to a substantially longer-wavelength forebulge than for a lithosphere which is weak at depth. This can be seen by the 60–80 km apparent thicknesses displayed for a lithosphere with a 10^{24} Pa s lower lithosphere (Fig. 5).

The apparent elastic thickness of the lithosphere depends on the age of the lithosphere, as shown with four other cases corresponding to lithospheres that are 13.5, 24, 54 and 96 Myr old. The thickness of the lower and the upper lithosphere in these cases differed from the reference model, while all other parameters remained the same (including lithosphere viscosities). The apparent elastic thickness of the lithosphere is a function of the age of the lithosphere (Fig. 6).

The influence of the fault dip angle, θ_F, and slab dip angle, θ_S, were also investigated. Two models with fault dip angles of 20° and 45° (compared to 30° in the reference model) were computed, as well as two models with slab dip angles of 45° and 90° (compared to 60° in the reference model). It appears that when θ_F is large (when the fault is more nearly vertical), the displacement of the fault is larger, the trench is deeper, and the back-arc basin depth is lower. Faults that are closer to the vertical lead to more efficient coupling between the negative buoyancy of the slab and the top surface of the subducting plate. This result is consistent with the viscous models of Zhong & Gurnis (1994), where the dynamic topography is assumed to be always in equilibrium with the viscous stresses.

The apparent elastic thickness after 5 Myr is independent of the fault dip angle, but the timescale for T_e relaxation is longer for larger fault dips. The timescale is 0.6 Myr when $\theta_F = 20°$, 0.9 Myr when $\theta_F = 30°$ and 1.5 Myr when $\theta_F = 45°$. A shallower-dipping fault produces less vertical stress close to the fault, making it easier for the subducting plate to slip under the overriding plate. The time necessary to relax those stresses is shorter. In terms of the influence of deeper slab structure, however, the apparent elastic thickness inferred for trench–forebulge topography is independent of slab dip angle.

The velocity field within the mantle is dependent on the dip angle of the slab, θ_S. The back-arc basin depth depends strongly on the slab dip angle, while trench depth varies only slightly. Both depths are larger when the slab is vertical, because the vertical stresses are more localized. Similar to the prediction from the Zhong & Gurnis (1994) viscous models, the trench depth depends more on fault dip angle than slab dip angle.

3.3 Influence of trench-rollback and continuous subduction

In order to determine if continuous subduction and trench rollback influence the relaxation of topography, two additional calculations were carried out with the model set-up described above. In one case the equilibrium dynamic topography was calculated (e.g. free-slip top), while in the second a free-surface was used with the pseudo-free-surface method. All other parameters were the same.

With an initial configuration of buoyancy consisting of a simple conductive boundary layer in the ocean, but with no slab, the continent moves oceanwards along with the converging

margin; subduction quickly develops in this model (e.g. Zhong & Gurnis 1995a). After 9 Myr, the subducting slab reaches a depth of 250 km for both the free-slip and free-surface cases; and the plate margins have migrated by about 400 km and 450 km for free-slip and free-surface cases, respectively (Fig. 7). At 21 Myr, the slab enters the lower mantle with a relatively shallow dip angle for both free-slip and free-surface cases (Fig. 8) and the plate margins have moved by about 1000 km and 1070 km for the free-slip and free-surface cases, respectively (Figs 7 and 8). Compared with the free-slip case, the free-surface case yields a topographically broader and shallower back-arc basin with a significant bulge at a distance of about 800 km for the trench (Figs 7a and c). Trenches from the free-surface case are deeper but of a similar width compared with the case where the equilibrium dynamic topography assumption is made.

The surface relaxation has a significant influence on the back-arc topography above the subducting slab (Fig. 7). The

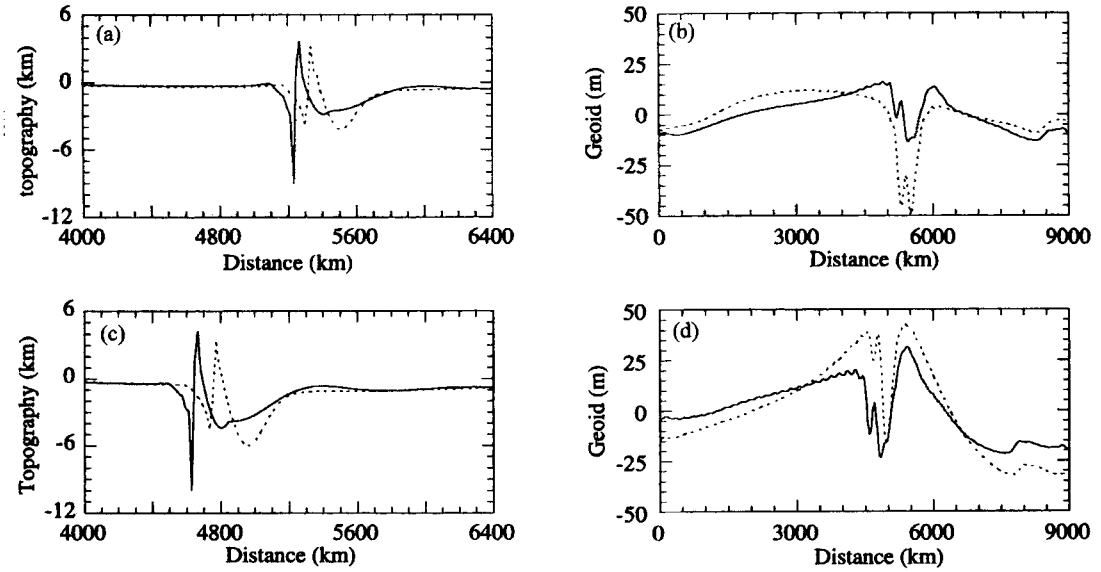

Figure 7. Dynamic topography and geoid at 9 Myr (a and b) and at 21 Myr (c and d). The solid and dashed lines are for free-surface and free-slip models, respectively.

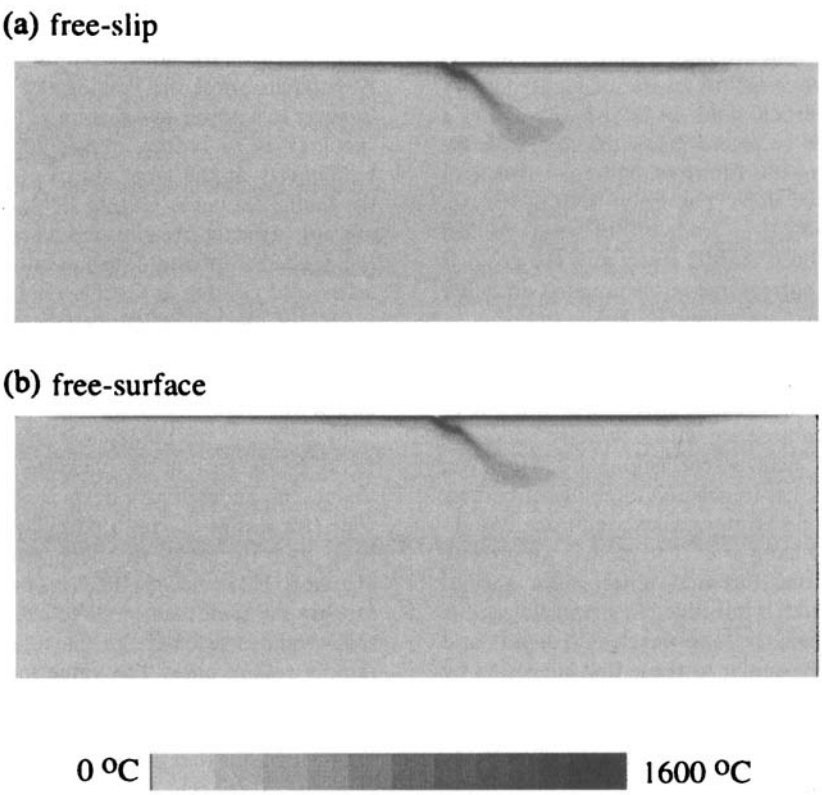

Figure 8. Thermal structure for subducted slabs from (a) free-slip and (b) free-surface models at 21 Myr.

shallower back-arc topography in the free-surface case is due to the filtering out of the relatively short-wavelength components of topography. The higher-frequency components require longer periods of time to grow (Part I), and for O (100 km) scales this timescale is longer than the timescale of slab retreat. The broader back-arc topography may result from the relatively slow rebound of surface topography after the slab retreats (Fig. 7).

Care must be taken in the interpretation of trench depth from the free-surface case. Since the deepest part of the trench has a very sharp topography (Fig. 7), it is unclear whether or not our pseudo-free-surface techniques will be valid in the limit of a relatively large ratio of topographic amplitude to wavelength within the trench. However, we note that the part of the trench where topography varies gradually is similar between these two cases (Fig. 7). In these non-Newtonian calculations, boundary conditions have a relatively strong influence on flow field because of the feedback into the rheology. This may explain the faster motion of plate margins in the free-surface case.

4 DISCUSSION AND CONCLUSIONS

The models presented here simultaneously match observed long- and short-wavelength features of converging margins reasonably well. On a long-wavelength scale, we have been able to reproduce the geoid high observed over slabs. Simultaneously, we have been able to reproduce the finer-scale features of trenches, in particular trench depth and forebulge morphology. These features are dependent both on time and on the details of vertical viscosity stratification. The primary discrepancy between our models and the Earth is that observed back-arc basins are shallower and broader.

We are able to reproduce long-wavelength geoid highs ($\sim$20–40 m over $>$5000 km) when there is a jump in viscosity between the upper and lower mantle. The mechanism is identical to the original viscous-flow model of Hager (1984); at long wavelengths the vertical gradient in viscosity causes a greater fraction of stress to be placed below the slab, with the consequence of there being less (downward) long-wavelength dynamic topography above slabs. The heavy slab dominates the long-wavelength geoid. The trade-off between vertical viscosity stratification at deep mantle levels and the geoid is not any different in the current models compared to other purely viscous formulations [see review by King (1995)].

We propose a scenario for forebulges qualitatively similar to that proposed by Melosh (1978): the forebulge is the result of viscous flow in the lower oceanic lithosphere. Melosh & Raefsky (1980) studied this problem with a velocity boundary condition imposed on a bent viscoelastic plate. However, Zhang *et al.* (1995) argued that trench and forebulge structures were dependent on the imposed boundary conditions. We do not dispute the results of Zhang *et al.* The models we present, however, use realistic geometries and much more natural boundary conditions (the slab is imbedded in a realistic viscous mantle, allowing us to explain the long-wavelength geoid), and we find results qualitatively similar to those first suggested by Melosh (1978). Moreover, based on the comparison of effective mechanical thicknesses at seamounts and trenches, the viscosity of the lower lithosphere may be about 10^{23} Pa s, but probably smaller than about 10^{24} Pa s. A 10^{24} Pa s lower lithosphere produces forebulges that are too wide and hence too thick (Fig. 5) compared with observed effective elastic thicknesses (e.g. Watts *et al.* 1980). Our constraint is consistent with the 10^{24} Pa s nominal value proposed by Melosh (1978). One of the primary reasons Melosh (1978) argued for dynamic support of the outer rise by viscous flow was the relatively low stresses needed compared with the large fibre stresses generated in thin-elastic-plate models. Again, the stresses modelled in these continuum models are quite similar: about 5 MPa (50 bars) normal stress in the vicinity of the forebulge and $\sim$100 MPa ($\sim$ a kilobar) at the trench. The high stresses are consistent with the normal faulted morphology of trenches. High stresses in the lithosphere below the trench are consistent with the implicit requirement needed to weaken the plate margin. A weak plate margin allows the plate to bend at the trench and subduct.

The elastic thickness versus the age of the lithosphere shown for three different integration times are compared with the elastic thicknesses calculated at oceanic trenches and seamounts (Fig. 6). A fundamental attribute of buoyancy-driven, viscoelastic models is that oceanic lithosphere appears thicker at short timescales (less than about one million years). For a convergence rate of 10 cm yr^{-1}, the oceanic lithosphere moves from forebulge to trench on average in less than 1.5 Myr. This produces a straightforward explanation for the dilemma discussed by Wessel (1992) that oceanic lithosphere appears thicker at trenches but thinner at seamounts. Seamounts load the lithosphere for timescales substantially greater than five million years and consequently all elastic stresses within the lower lithosphere should have relaxed. In the oceanic trench environment, the forebulges are dynamically maintained by viscous stresses in the lower lithosphere and mantle.

Trenches are generally not deeper than 5 km, but we often find that trenches deepen beyond this for model times greater than a few million years. This discrepancy between modelled and observed bathymetry may be the result of several approximations. The rheology used in our viscoelastic models is Newtonian, while the rheology of the lithosphere and mantle is closer to a power-law rheology. The influence of this different rheology is to reduce trench depth and to smooth trench bathymetry at the large stresses ($\sim$1 kbar) in the vicinity of the fault (Zhong & Gurnis 1994). On the other hand, faults are not perfectly free-slip and when resistive shear stresses on the fault are present, displacements and trench depth are attenuated (Zhong & Gurnis 1994).

Finally, one primary drawback of the present models is that back-arc basins are both too narrow and too deep in the models compared to back-arc basins in the Pacific. Back-arc basins are about 500 m anomalously deep when corrected for both the age of the lithosphere and a thinner crust (see Gurnis 1993). In the case of the back-arc basins west of the Mariana trench, the anomalously deep regions are more than 1000 km wide (Moresi & Gurnis 1996). The Mariana trench is rolling back and so some transient relaxation of topography is expected. However, we find that the transient relaxation of topography is not sufficient to cause broadening and relative shallowing as extensive as that observed above a slab that is rapidly rolling back. The value for the viscosity of the overriding plate which we use, 10^{25} Pa s, is much too large based on the above constraint from forebulge morphology. It leads to back-arc basins that are only about 600 km wide versus 400 km wide and 30 per cent shallower for the free-surface formulation of dynamic topography compared to the equilibrium formu-

lation. Clearly, trench rollback and viscous relaxation cannot fully solve the dilemma of excessive dynamic topography above back-arc basins predicted by viscous models of subduction.

The narrow geoid low over the back arc has persisted in the free-surface formulation although diminished for some cases with the viscoelastic formulation. We can ony conclude that a significant component of the physics causing compensation is still missing. This missing piece may be related to partial melting occurring beneath the back arc (for example in the wedge). Certainly, the perturbation in seismic velocity of the wedge, presumably caused by partial melting, dominates over the cold slab in tomographic inversions of the upper mantle (Nakanishi & Anderson 1984; Woodhouse & Dziewonski 1984; Anderson, Tanimoto & Zhang 1993). Indeed, the wedges are seismically slow, consistent with the possibility that there is additional density or buoyancy there. Despite these limitations, we believe that free-surface formulations with faults have nearly closed the gap between flexural and geodynamic approaches of subduction-zone dynamics.

ACKNOWLEDGMENTS

We thank John Toth for a helpful review. This paper is contribution number 5617 of the Division of Geological and Planetary Sciences, California Institute of Technology. The TECTON finite-element software used here was provided by H. J. Melosh of The University of Arizona. The work was supported by the David and Lucile Packard Foundation and NSF grants EAR-9496185 and EAR-9417645.

REFERENCES

Anderson, D.L., Tanimoto, T. & Zhang, Y.-S., 1992. Plate tectonics and hotspots: the third dimension, *Science,* **256,** 1645–1651.

Caldwell, J.G., Haxby, W.F., Karig, D.E. & Turcotte, D.L., 1976. On the applicability of a universal elastic trench profile, *Earth planet. Sci. Lett.,* **31,** 239–246.

Cathles, L.M., 1975. *The Viscosity of the Earth's Mantle,* Princeton University Press, Princeton, NJ.

De Bremaecker, J.-C., 1977. Is the oceanic lithosphere elastic or viscous, *J. geophys. Res.,* **82,** 2001–2004.

Grellet, C. & Dubois, J., 1982. The depth of trenches as a function of the subduction rate and age of lithosphere, *Tectonophysics,* **82,** 45–56.

Griggs, D.T., 1972. The sinking lithosphere and the focal mechanisms of deep earthquakes, in *Nature of the Solid Earth,* pp. 361–384, eds Robertson, E.C., Hays, J.F. & Knopoff, L., McGraw-Hill Company, Inc., New York, NY.

Gurnis, M., 1993. Depressed continental hypsometry behind oceanic trenches: a clue to subduction controls on sea level change, *Geology,* **21,** 29–32.

Hager, B.H., 1984. Subducted slabs and the geoid: constraints on mantle rheology and flow, *J. geophys. Res.,* **89,** 6003–6015.

Heiskanen, W.A. & Vening Meinesz, F.A., 1958. *The Earth and its Gravity Field,* McGraw-Hill Book Company, Inc., New York, NY.

Hilde, T.W.C. & Uyeda, S., 1983. Trench depth: variation and significance, in *Geodynamics of the Western Pacific–Indonesian Region,* Geodyn. Ser. 11, pp. 75–89, eds Hilde, T.W.C. & Uyeda, S., Am. geophys. Un., Washington, D.C.

Jarrard, R.D., 1986. Relations among subduction parameters, *Rev. Geophys.,* **24,** 217–284.

Kaula, W.M., 1972. Global gravity and tectonics, in *The Nature of the Solid Earth,* pp. 385–405, eds Robertson, E.C., Hays, J.F. & Knopoff, L., McGraw-Hill Company, Inc., New York, NY.

King, S.D., 1995. The viscosity structure of the mantle, *Rev. Geophys. Suppl. U.S. National Report to IUGG, 1991–95,* 11–17.

McAdoo, D.C., Caldwell, J.G. & Turcotte, D.L., 1978. On the elastic-perfectly plastic bending of the lithosphere under generalized loading with application to the Kuril trench, *Geophys. J. R. astr. Soc.,* **54,** 11–26.

McAdoo, D.C., Martin, C.F. & Poulouse, S., 1985. Seasat observations of flexure: evidence for a strong lithosphere, *Tectonophysics,* **116,** 209–222.

Melosh, H.J., 1978. Dynamic support of the outer rise, *Geophys. Res. Lett.,* **5,** 321–324.

Melosh, H.J. & Raefsky, A., 1980. The dynamical origin of subduction zone topography, *Geophys. J. R. astr. Soc.,* **60,** 333–354.

Melosh, H.J. & Williams, C.A., 1989. Mechanics of graben formation in crustal rocks: a finite element analysis, *J. geophys. Res.,* **94,** 13 961–13 973.

Moresi, L. & Gurnis, M., 1996. Constraints on the lateral strength of slabs from three-dimensional dynamic flow models, *Earth planet. Sci. Lett.,* **138,** 15–28.

Nakanishi, I. & Anderson, D.L., 1984. Aspherical heterogeneity of the mantle from phase velocities of mantle waves, *Nature,* **307,** 117–121.

Parsons, B. & Molnar, B., 1976. The origin of outer topographic rises associated with trenches, *Geophys. J. R. astr. Soc.,* **45,** 707–712.

Turcotte, D. & Schubert, G., 1982. *Geodynamics,* John Wiley, New York, NY.

Walcott, R.I., 1970. Flexural rigidity, thickness, and viscosity of the lithosphere, *J. geophys. Res.,* **75,** 3941–3954.

Watts, A.B. & Talwani, M., 1974. Gravity anomalies seaward of deep-sea trenches and their tectonic implications, *Geophys. J. R. astr. Soc.,* **36,** 57–90.

Watts, A.B., Bodine, J.H. & Ribe, N.M., 1980. Observations of flexure and the geological evolution of the Pacific Ocean Basin, *Nature,* **283,** 532–537.

Wessel, P., 1992. Thermal stresses and the bimodal distribution of elastic thickness estimates of the oceanic lithosphere, *J. geophys. Res.,* **97,** 14 177–14 193.

Woodhouse, J.H. & Dziewonski, A.M., 1984. Mapping the upper mantle: three-dimensional modeling of Earth structure by inversion of seimsic waveforms, *J. geophys. Res.,* **89,** 5953–5986.

Zhang, J., Hager, B.H. & Raefsky, A., 1985. A critical assessment of viscous models of trench topography and corner flow, *Geophys. J. R. astr. Soc.,* **83,** 451–475.

Zhong, S. & Gurnis, M., 1992. Viscous flow model of a subduction zone with a faulted lithosphere: long and short wavelength topography, gravity, and geoid, *Geophys. Res. Lett.,* **19,** 1891–1894.

Zhong, S. & Gurnis, M., 1994. Controls on trench topography from dynamic models of subducted slabs, *J. geophys. Res.,* **99,** 15 683–15 695.

Zhong, S. & Gurnis, M., 1995a. Mantle convection with plates and mobile, faulted plate margins, *Science,* **267,** 838–843.

Zhong, S. & Gurnis, M., 1995b. Towards a realistic simulation of plate margins in models of mantle convection, *Geophys. Res. Lett.,* **22,** 981–984.

Zhong, S., Gurnis, M. & Moresi, L., 1996. Free-surface formulations of mantle convection—I. Basic theory and application to plumes, *Geophys. J. Int.,* **127,** 708–718 (this issue).